Athanasios Zisis, Norman A. Fleck
Cambridge University Engineering Dept., Cambridge, UK

Mechanisms of elastodynamic erosion of electron-beam thermal barrier coatings

Dedicated to Professor A. G. Evans on the occasion of his 65th birthday

The elastodynamic response of a columnar thermal barrier coating to normal impact by a spherical particle is explored using an explicit finite element method. The transient stress state involves a tensile component at the edge of each column, and this may lead to erosion. The contact problem can be simplified to the impact of a single column by an inclined wedge. The peak tensile stress is determined as a function of geometry of column and level of friction between wedge and columns. The initiation of a crack from a pre-existing flaw within the column is explored. The implications of the various calculations are discussed for erosion of thermal barrier coatings.

Keywords: Thermal barrier coatings; Finite element analysis; Erosion; Fracture mechanics; Dynamic loading

1. Introduction

The current generation of thermal barrier systems used in gas turbines comprise a stack of multifunctional layers. Electron beam deposited (EB-PVD) thermal barrier coatings (TBCs) have an outermost thermal barrier layer of yttria-stabilised-zirconia (YSZ), with an underlying thermally grown oxide (TGO) to give oxidation resistance. The YSZ layer is composed of discrete columns of diameter about 10 μm. Gaps between the columns endow the coating with strain compliance. The TGO grows progressively during the life of the coating by the oxidation of an aluminium-rich underlying bond coat, and the bond coat rests upon a substrate made from a nickel-based superalloy, see for example [1–3].

Thermal barrier systems exhibit two major categories of failure: one based on oxidation [1, 4–7] and the other on impact by projectiles ingested into the gas stream [8–10]. The models of oxidation-induced failure have reached a maturity that allows trends with constituent properties to be ascertained. The situation is less complete for failure mechanisms caused by impact. Turbine blades have a tip velocity of the order of 300 m s^{-1}, and suffer erosive wear under the impact of small erodent particles that move in the hot gas stream in the turbine, see [11–13]. Little information exists in the literature on the mechanisms that govern erosion of TBCs. At least two thermo-mechanical responses have been identified and are outlined as follows.

1.1. Severe erosion, also called foreign object damage (FOD)

Large particles at high velocity cause the material to be susceptible to large-scale plastic deformation and densification around the contact site. The deformation zones develop over millisecond timescales, as the impacting particle decelerates and then rebounds [8]. Within the densified zone, kink bands form and extend diagonally downward toward the interface with the TGO. In some cases, the bands reach the interface with the TGO and lead to delamination within the TBC, just above the TGO. Such delaminations provide a mechanism for creating large-scale spalls.

1.2. Mild erosion

During initial impact, elastic waves are induced in the TBC columns (Fig. 1). Over a time frame of nanoseconds, bending waves are induced at the tops of the columns, and these cause flaws at the column perimeter to extend across the columns. The column-sized cracks link, leading to small amounts of material removal. Note that the observed cracking pattern of Fig. 1 differs from Herztian cone cracking in a homogeneous half-space.

Welmann and co-workers [10, 14] have demonstrated the existence of the above two mechanisms of erosion. Experimental evidence on actual engine hardware and during accelerated testing confirms that the small particles lead to crack formation at various locations within the columnar zirconia top layer [13].

The focus of the current study is on the elastodynamic response of the thermal barrier coating upon normal impact by a spherical particle. Finite element (FE) simulations are used to quantify the transient stress state in the coating after impact, and to determine the crack tip loading on pre-existing flaws, leading to mild erosion. Several idealisations are made to bring out the essential features of the problem. In reality, particles impact at an inclination to the TBC surface, and the incoming particles are angular in shape. These refinements are, however, beyond the scope of the present study.

Some previous mechanics analyses have been performed on elastodynamic stress wave propagation from a travelling load at high velocity, see Johnson [15] and Freund [16] for reviews. The problems of a moving line load on an elastic half-space [17] and a high speed, rolling and sliding cylinder

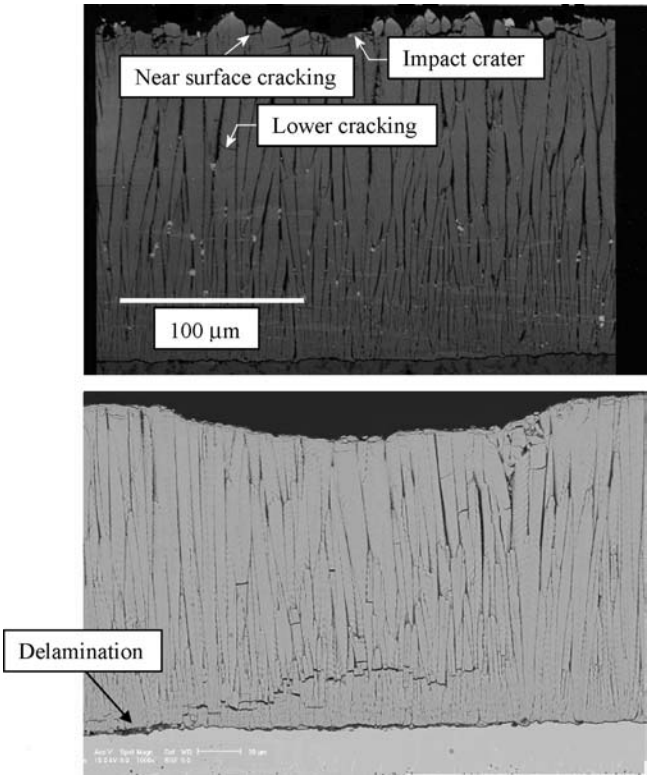

Fig. 1. (a) Scanning electron microscope image of specimen cross-section revealing the near-surface cracking of columns due to impact (Courtesy of J.R. Nicholls, Cranfield University). (b) Cracking at the bottom of the columns and delamination caused by a stress wave reaching the TBC/TGO interface (courtesy of A.G. Evans, UCSB).

[18] have both been addressed. In each case, as the velocity of the travelling load approaches the speed of elastic wave propagation the level of contact stress increases sharply due to material inertia. When the load travels supersonically, a sharp shock wave radiates from the contact point.

1.3. Outline of the study

The paper is structured as follows. First, a dynamic analysis is given of the normal impact of a set of TBC columns by a spherical particle. The presence of gaps between the columns causes them to behave independently in the early stages of contact with the particle, and so a much simpler side-problem is considered: the impact of a single column by a wedge indenter. The elastodynamic response of the single column is explored in detail, and the onset of cracking near the surface is considered.

2. Normal impact of a TBC layer by a spherical particle

A preliminary set of finite element calculations is now reported for the normal impact by a rigid spherical particle upon a columnar layer of TBC. The initial elastodynamic response is explored (on a timescale of nanoseconds), and for our present purposes there is no need to model each underlying layer explicitly. This analysis builds upon the previous study by Chen et al. [12], and is used to motivate the calculations performed in subsequent sections of the paper.

2.1. Material and geometric parameters

A representative normal impact event is simulated with the following choice of material and geometric parameters. A rigid sphere of radius $R = 25\ \mu m$ and density $\rho_P = 2000\ kg\ m^{-3}$ impacts the TBC layer at an initial velocity $V = 300\ m\ s^{-1}$. After impact, the contact loading on the particle causes it to retard and rebound from the TBC layer. The TBC comprises columns of height $H_{TBC} = 200\ \mu m$, width $d = 10\ \mu m$ and intervening gap of width $g = 0.1\ \mu m$. The columns have a Young's modulus $E_{TBC} = 140$ GPa, Poisson's ratio $\nu = 0.3$ and density $\rho_{TBC} = 5900\ kg\ m^{-3}$, and are adhered to a rigid substrate. Frictionless contact is assumed between the columns and for contact between the rigid sphere and top of columns.

2.2. Finite element simulations

In order to generate a tractable problem, an axisymmetric finite element model is constructed, with the columnar microstructure represented by concentric hollow circular cylinders of wall width d and intervening gap width g. This idealisation has been used previously to model the indentation of a TBC coating [12]. A cylindrical coordinate system is adopted with radial co-ordinate x_1 and axial co-ordinate x_2, see Fig. 2.

The commercial finite element program ABAQUS Explicit (version 6.2) was employed. A mesh sensitivity study revealed that adequate accuracy is achieved using 160 000 4-noded quadrilateral, axisymmetric elements (CAX4R in ABAQUS). The displacement boundary conditions are $u_1 = 0$ along the axis of symmetry, a clamped condition $u_1 = u_2 = 0$ along the bottom of the mesh, and a traction-free side boundary. Numerical experimentation confirmed that a mesh of radial extent 250 μm is adequate to capture the initial elasto-dynamic response: we are interested in

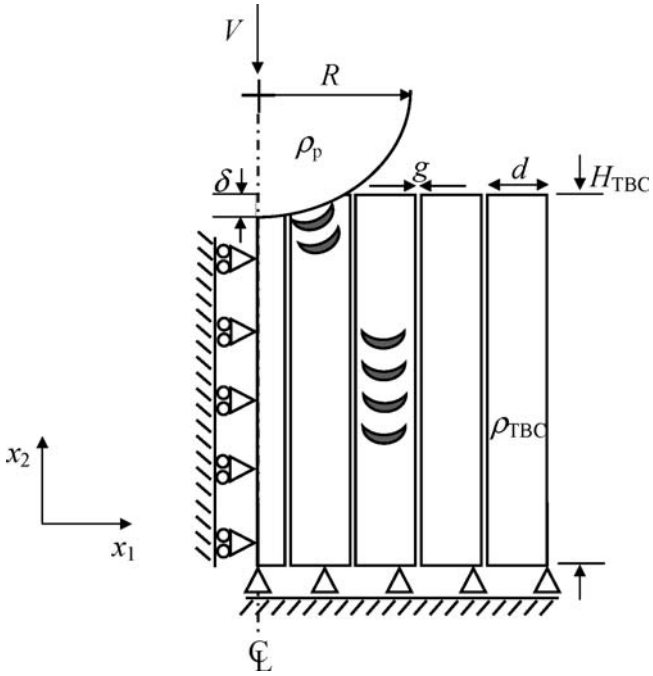

Fig. 2. A spherical projectile cracks the EB-PVD TBC columnar structure due to tensile stress wave propagation. The assumed boundary conditions are shown.

the response before stress waves reach the radial boundary of the mesh. Thus, the precise boundary conditions are unimportant for this boundary, and a traction-free condition is assumed for simplicity.

Small deformations and small strains are assumed: numerical checks confirmed that finite strain effects are negligible. Automatic time-stepping was performed with the Courant condition on time steps automatically satisfied. The default value of material viscosity in ABAQUS was used throughout.

2.3. A typical elastodynamic response

It is instructive to explore the evolution in stress state after impact of the TBC coating by a rigid sphere. This will motivate the subsequent study. Contours of axial tensile stress are shown in Fig. 3 at selected times after impact. Only tension is shown, with white indicating axial compression. To a first approximation, the columnar layer behaves as an array of independent wave-guides. Immediately following impact a combination of longitudinal, shear and Rayleigh waves emanate from the contact into the central column. After $t = 1$ ns a local maximum tensile stress of 1.4 GPa is attained at the side-surface of the central column, and at a depth of 2 μm below the surface of the coating (denoted by point A in Fig. 3). The first column contacts the second column after $t = 2$ ns. Contact between the sphere and the second column is established after 3 ns and the ensuing response is similar to the initial behaviour of the first column: longitudinal, shear and Rayleigh waves travel across the width d of the second column. Tensile stresses build up within the second column and attain a maximum value of 3.9 GPa at the right-hand boundary of the column after $t = 7$ ns (point B). The depth at which the stress peaks is 5 μm, which is equal to half the width of the columns.

The second column laterally impacts the third column and elastic waves propagate within the third column. These waves reach the right-hand boundary of the column, and then propagate axially down the column. Note that contact with the sphere extends only to the first two columns and rebound occurs before contact is established with the third column. Thus, propagation of stress waves into the third column is only due to contact between the second and third columns.

At $t = 12$ ns, the tensile axial stress peaks at the periphery of the third column (point C), and moves down to point D after 15 ns. The sphere separates from the TBC layer and rebounds after 19 ns. Tensile waves continue to travel down the third column so that the spatial maximum over all columns is at point E after 40 ns. After 50 ns the tensile stress waves in the third column reach the lower interface between the TBC layer and the rigid substrate and are then reflected back into the TBC layer. Simultaneously, compressive waves move down the first two columns and are reflected back as tensile waves from the rigid substrate.

It is instructive to plot the maximum spatial value of tensile stress within the TBC layer as a function of time, see Fig. 4. We emphasise that the location of peak stress varies with time, and the intent of the figure is to seek out the maximum stress anywhere in the coating and thereby assess the likelihood of failure. The maximum value is at point A after

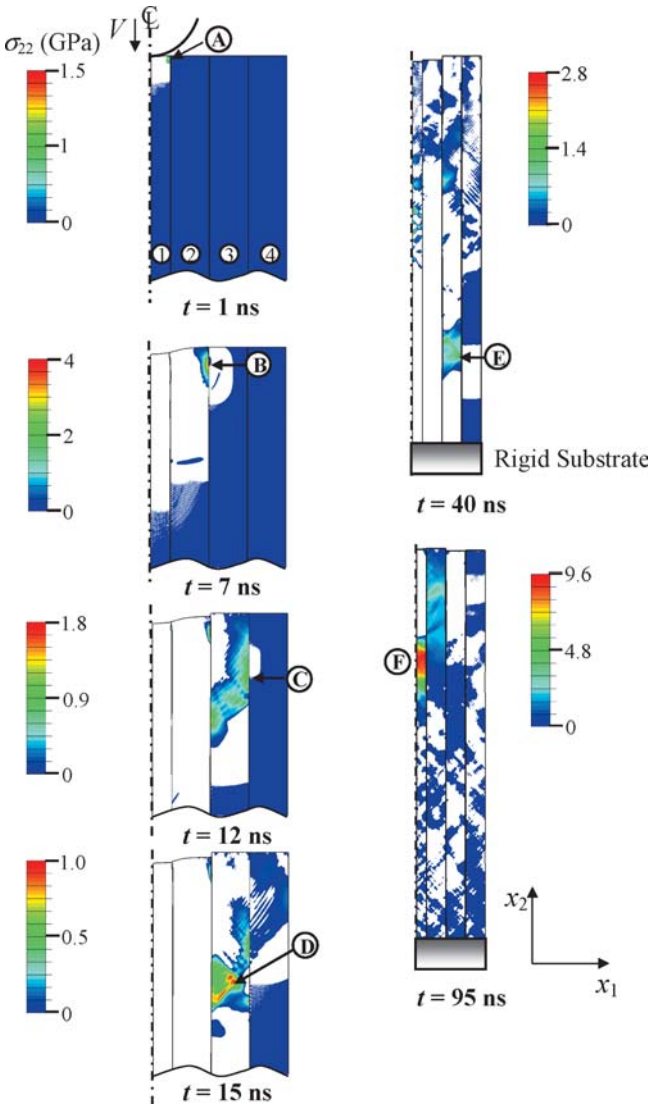

Fig. 3. Time sequences of contours of tensile stress σ_{22} (GPa) within the first four columns from the collision point. Only tension is shown and the colour white corresponds to compression. ($g = 0.1$ μm, $V = 300$ ms^{-1}, $E_{TBC} = 140$ GPa, $\rho_{TBC} = 5900$ kg m^{-3}, $\rho_P = 2000$ kg m^{-3}, $g = 0.1$ μm, $\mu_c = \mu_s = 0$).

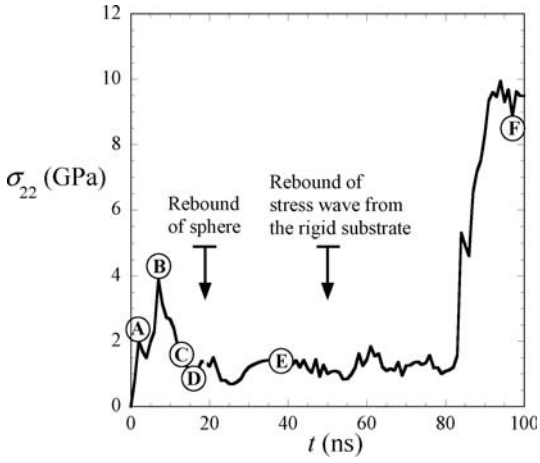

Fig. 4. Tensile stress history of the first four first columns from the collision point. Global maximum tensile stress is reported as a function of time for gap width $g = 0.1$ μm. ($V = 300$ m s^{-1}, $E_{TBC} = 140$ GPa, $\rho_{TBC} = 5900$ kg m^{-3}, $\rho_P = 2000$ kg m^{-3}, $\mu_c = \mu_s = 0$).

1 ns and moves to point B after 7 ns, as discussed above. The maximum stress is of the order of 1–4 GPa for the first 85 ns. Then, the tensile stress is intensified in the central column to about 10 GPa, see for example point F of Fig. 3 at 95 ns.

Numerical experiments have been performed to explore the sensitivity of the above stress history to the gap width g and to the level of Coulomb friction (μ_c, μ_s). The gap g is varied from 0.1 μm to 1 μm, and the friction coefficients are varied from zero to unity. The transient stress levels drop slightly with increasing friction, but increase with increasing gap width. However, the above qualitative discussion and conclusions remain and so it is unnecessary to present detailed results here.

2.4. Cracking criterion

The feathery edges of the columns contain crack-like flaws of length a about 1 μm [12]. It is postulated that the transient tensile stress after impact is sufficient to crack the columns. An initial assessment is made here of the magnitude of stress intensity factor generated at the tip of a putative crack in the column.

Consider again the elastodynamic response of the array of columns shown in Fig. 2. A few nanoseconds after impact by the spherical projectile, a tensile stress of about 1.4 GPa is attained at the side face of the impacted column 1. This is shown as point A in Figs. 3 and 4. Now impose this high stress on an edge crack of length $a = 1$ μm in the column. The level of mode I stress intensity factor generated by this loading is on the order of $K \approx \sigma_{max}\sqrt{\pi a} = 2.5$ MPa $\sqrt{m}$. Similarly, after about 7 ns the tensile stress peaks in the second column (at point B of Fig. 3), and generates a stress intensity factor of magnitude $K \approx 7$ MPa $\sqrt{m}$ for a putative edge crack of length $a =$ 1 μm in this column. These peak values of stress intensity factor at points A and B exceed the estimated fracture toughness $K_{TBC} \approx 1$ to 3 MPa $\sqrt{m}$ (Evans and co-workers [3]) of the TBC layer and consequently lead to crack advance across the columns. At later times, the tensile stress wave moves down the columns, and other tensile waves reflect up the central column: the propagation of edge cracks across the columns is again expected.

3. The unit event: dynamic loading of a single column by a wedge

An inspection of Fig. 4 reveals that, over the first 80 ns, the first and second columns of the TBC coating undergo the highest stressing of the coating. They suffer these high stresses on a timescale of several nanoseconds following impact, and during this period they behave essentially as independent columns in contact with the rigid sphere. It is now shown that the response of each TBC column can be estimated from the behaviour of a two dimensional single column impacted by a wedge of inclination α, as defined in Fig. 5. The wedge angle mimics the contact angle at the periphery of contact between a spherical particle and TBC layer: this contact angle increases with increasing contact size. Finite element simulations are now reported for the idealised unit impact event of a single column by a wedge.

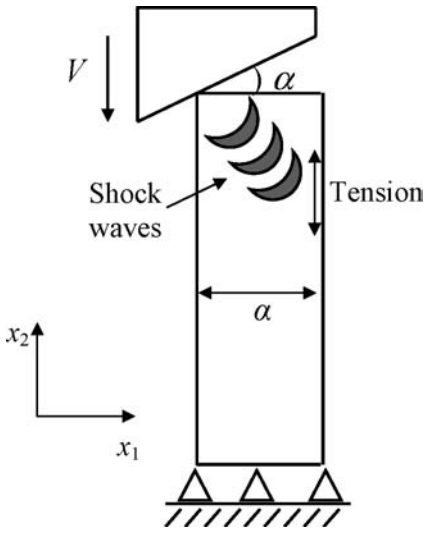

Fig. 5. Isolated single column impacted by a wedge of velocity V and inclination α. Elastic stress waves emanate from the contact and produce a high tensile stress at the opposing side boundary of the column.

3.1. Finite element simulations of wedge impact upon a single TBC column

Consider the problem of a single TBC column impacted by a rigid wedge of inclination α at a constant velocity V. The finite element program ABAQUS Explicit version 6.2 was again used to determine the dynamic response. Due to computational limitations, 2D plane strain simulations were performed, with the TBC columns of width $d = 10$ μm and $H_{TBC} = 150$ μm modelled by 120 000 4-noded reduced integration quadrilaterals (element type CPE4R in ABAQUS). The column is modelled as an isotropic, linear elastic solid with a Young's modulus E_{TBC} of 140 GPa and a Poisson ratio ν of 0.3. For this choice of Poisson's ratio, the longitudinal wave speed is $c_1 = 1.16c$, the shear wave speed is $c_2 = 0.62c$, and the Rayleigh wave speed is $c_R = 0.57c$, in terms of the one dimensional wave speed $c = \sqrt{E_{TBC}/\rho_{TBC}}$.

Both frictionless contact and Coulomb friction between wedge and column are considered. Automatic time-stepping was employed such that the Courant condition on time steps was satisfied automatically. The default value of material viscosity was used throughout. Continuity dictates that the contact point velocity V_p between the wedge and upper surface of the column is related to the impact velocity V by

$$V_p = V \cot \alpha \tag{1}$$

Note that V_p can be arbitrary large for sufficiently small α. For the case of an inclined wedge, α is constant. In contrast, in the initial stages of contact between a round particle and a flat half-space, the angle of attack α is small, and the contact point initially travels supersonically at $V_p > c_1$. Subsequently, the contact radius enlarges, α increases and V_p drops in magnitude to subsonic values.

Three regimes of contact point velocity V_p exist: supersonic, transonic and subsonic depending upon the magnitude of V_p in relation to (c_1, c_2, c_R), see for example Brock and Georgiadis [19]. The contact point travels *supersonically* when V_p exceeds c_1, *transonic* motion pertains when

V_p is between c_2 and c_1, and subsonic motion occurs for $V_p < c_2$. Three sample calculations of wedge impact are now considered to contrast the qualitative nature of these three regimes.

(i) Supersonic regime: $V_p > c_1$

A supersonic response is represented by the choice $V = 1200$ m s^{-1} and $\alpha = 5^\circ$. This corresponds to $V_p = 2.8c$. Contours of axial stresses are shown in Fig. 6 at selected times after impact. Note that no tension is observed, but shock waves are formed at the contact point. Ahead of the contact the surface is undisturbed and behind it the surface is uniformly depressed. In this regime, full contact across the width of the column is soon established and the column acquires a one dimensional compressive pulse. No failure is anticipated.

(ii) Transonic regime: $c_2 < V_p < c_1$

Transonic behaviour occurs for an impact angle $\alpha = 5^\circ$ and a wedge velocity of $V = 300$ m s^{-1}. Consequently, we have $V_p = 0.69c$. The transonic regime is more complicated than the supersonic regime. The contact point travels supersonically with respect to the shear wave but subsonically with respect to the longitudinal wave. For the choice of $\nu = 0.3$, the Rayleigh wave speed c_R is close to the shear wave speed c_2. Contours of axial tensile stresses are shown in Fig. 7 at selected times after impact. A shear wave propagates ahead of the contact point with a peak value of $\sigma_{22} = 0.71$ GPa at $t = 1$ ns. The shear wave builds up and attains a maximum value of $\sigma_{22} = 6.62$ GPa at $t = 3.5$ ns at the right-hand side of the column. This tensile stress corresponds to a value of $0.8\rho_{TBC}cV$.

(iii) Subsonic regime: $V_p < c_2$

At an impact angle of $\alpha = 5^\circ$, and a wedge velocity, $V = 262$ m s^{-1} the contact point travels subsonically at $V_p = 0.61c$. A train of stress waves propagates from the contact point. The longitudinal waves propagate ahead of both the Rayleigh and shear waves. Contours of axial stress σ_{22} are given in Fig. 8. After $t = 3$ ns, the shear wave has reached the boundary of the column and $\sigma_{22} = 1.93$ GPa. The maximum value of $\sigma_{22} = 6.78$ GPa (corresponding to $0.9\rho_{TBC}cV$) is obtained at $t = 3.5$ ns and is again at the right-hand side of the column (Fig. 8).

Define the normalised tensile stress by $\bar{\sigma}_{22} = \sigma_{22}/\rho_{TBC}cV$. The spatial maximum of $\bar{\sigma}_{22}$ is plotted against time in Fig. 9, for the transonic case $V_p = 0.69c$ and subsonic case $V_p = 0.61c$. The times t_1, t_2 and t_R correspond to the travel time for the longitudinal wave, shear wave and Rayleigh wave, respectively, to span the column of width, d. For the transonic case of $V_p = 0.69c$ the spatial maximum tensile stress has a peak value of $(\bar{\sigma}_{22})_{max} = 0.8$ at a time $t_2 = 3.31$ ns. For the subsonic case of $V_p = 0.61c$, the tensile stress peaks at $t_R = 3.57$ ns with a value of $(\bar{\sigma}_{22})_{max} = 0.9$. This implies that the Rayleigh wave makes a dominant contribution to the transient stress at subsonic contact speeds.

Figure 10 presents the spatial and temporal maximum value of tensile stress $(\bar{\sigma}_{22})_{max}$ at the right-hand boundary of the column for each simulation, plotted as a function of

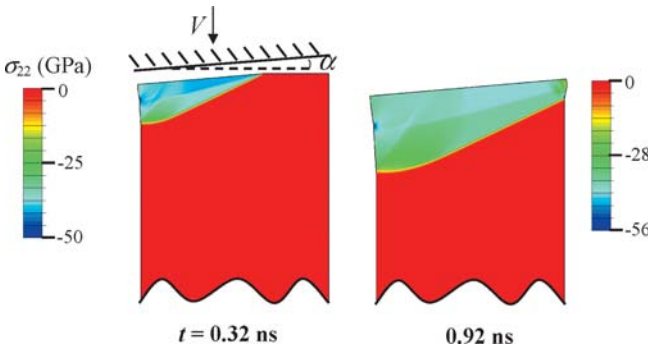

Fig. 6. Contours of axial stress σ_{22} at selected times after impact. The contact point has supersonic velocity $V_p = 2.8c$ ($V = 1200$ m s^{-1}, $\alpha = 5^\circ$, $E_{TBC} = 140$ GPa, $\nu = 0.3$).

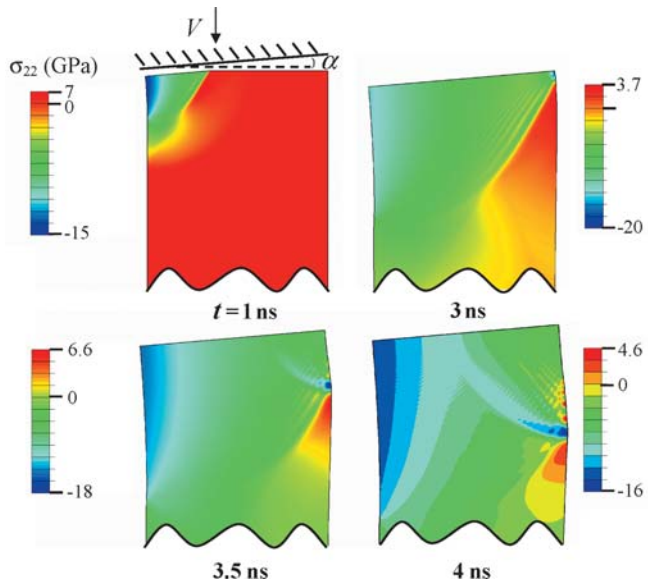

Fig. 7. Contours of axial stress, σ_{22}, at selected times after the impact. The contact point has transonic velocity $V_p = 0.69c$ ($V = 300$ m s^{-1}, $\alpha = 5^\circ$, $E_{TBC} = 140$ GPa, $\nu = 0.3$).

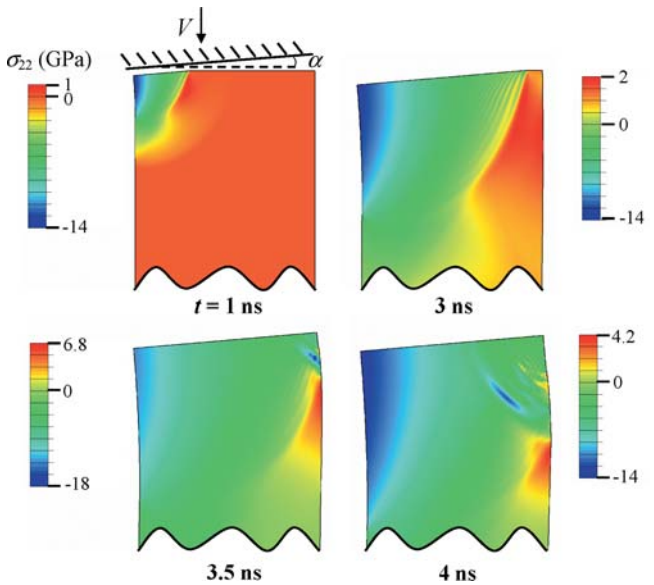

Fig. 8. Contours of axial stress, σ_{22}, at selected times after the impact. The contact point has subsonic velocity $V_p = 0.61c$ ($V = 262$ m s^{-1}, $\alpha = 5^\circ$, $E_{TBC} = 140$ GPa, $\nu = 0.3$).

the non dimensional contact velocity $\bar{V}_p = V_p/c$. Four curves are shown. In three cases, the inclination α is held fixed at $\alpha = 10^\circ$, 15° and 20°, and the velocity is varied from 72 m s^{-1} to 1750 m s^{-1}. For the fourth curve the velocity is held fixed at 300 m s^{-1} while the wedge angle is varied from 0.85° to 40°. We note from the figure that for small values of V_p, much below c_2, the values of $(\bar{\sigma}_{22})_{max}$ are small. This is the regime of quasi-static bending where stress wave effects are negligible. For $0.3 < \bar{V}_p < 1$ a plateau of constant normalised maximum tension, $(\bar{\sigma}_{22})_{max}$ of about unity is attained. In the supersonic regime, $V_p > c_1$, only compression develops within the column. This figure may be treated as a master plot of the elasto-dynamic response of a single column subjected to normal impact by an inclined wedge.

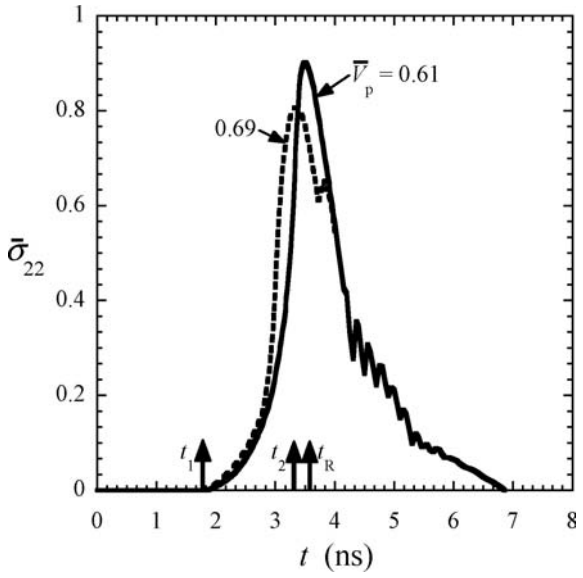

Fig. 9. Time history of the dimensionless axial tensile stresses at the right-hand boundary of the column for $V_p = 0.61c$, $0.69c$. For the choice $V_p = 2.8c$ no tension is observed. t_1, t_2 and t_R are the propagation times for longitudinal, shear and Rayleigh waves respectively to travel a distance d ($\alpha = 5^\circ$, $E_{TBC} = 140$ GPa, $\nu = 0.3$).

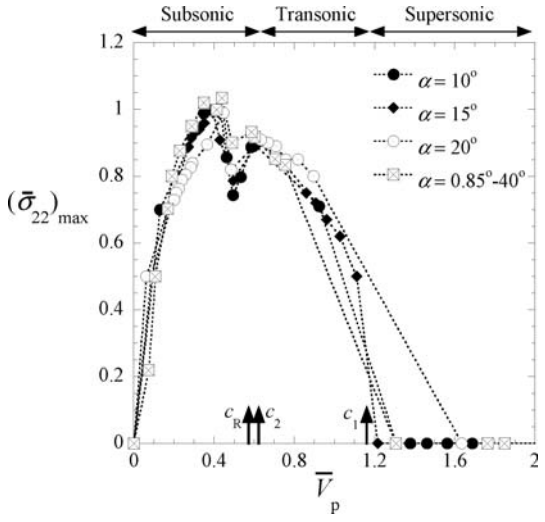

Fig. 10. Peak axial tensile stress $(\bar{\sigma}_{22})_{max}$ as a function of contact point velocity $\bar{V}_p$.

3.3. Effect of corner curvature upon peak tensile stress

TBC columns are not frictionless, right circular cylinders with flat tops. It is instructive to explore the sensitivity of the maximum tensile stress to the geometry of the upper surface of the column and to the level of Coulomb friction μ_s between the column and wedge. Numerical experimentation reveals that the friction level between the wedge and the surface of the column has only a minor effect upon the tensile stress at the boundaries of the columns and its effect can thus be neglected. (These calculations are omitted here for the sake of brevity.)

In order to explore the effect of radius of curvature of the tops of the TBC columns upon the induced stress waves, we replace the right-hand corner of the flat upper surface with a curved surface of local radius s as shown in Fig. 11. The peak tensile stress $(\bar{\sigma}_{22})_{max}$ is plotted as a function of $\bar{V}_p$ response for selected s in Fig. 12. At subsonic contact speeds

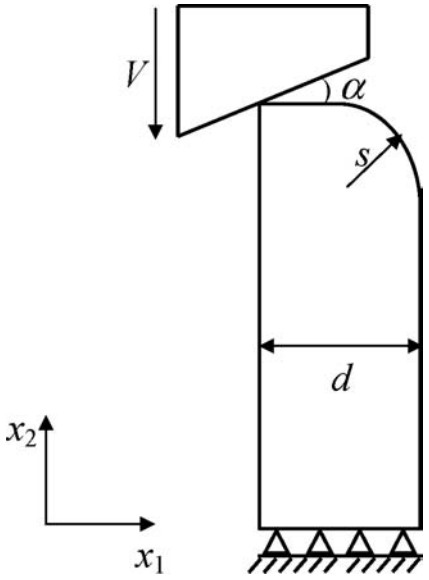

Fig. 11. Single column, with right hand corner of radius s, impacted by a wedge of angle α and at a constant velocity V.

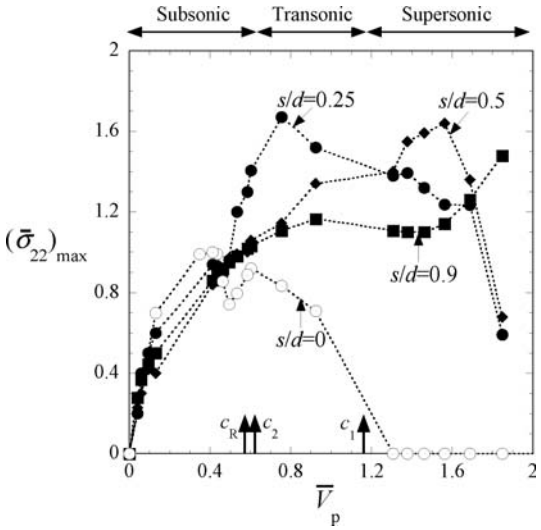

Fig. 12. The dependence of $(\bar{\sigma}_{22})_{max}$ upon $\bar{V}_p$, for selected values of radius of curvature s of the column. ($\alpha = 10^\circ$, $E_{TBC} = 140$ GPa, $\nu = 0.3$).

$(\bar{\sigma}_{22})_{\max}$ is almost insensitive to the value of s (over the range considered). But at higher contact speeds the peak stress increases with increasing s. The dependence is not monotonic. $(\bar{\sigma}_{22})_{\max}$ has a peak value of about 1.6 for all geometries with a curved corner, but the value of $\bar{V}_p$ corresponding to the maximum is sensitive to the value of s. This is due to the fact that the contact point velocity is not constant for the case of contact between a wedge and a curved surface. Due to the finite curvature, the effective wedge angle α increases as soon as the contact point reaches the curved corner, and consequently the contact point velocity decreases.

4. Concluding remarks

The elastodynamic response of TBC coatings due to impact by spherical particles has been evaluated in this study. It is found that the TBC columnar layer acts as a set of independent wave guides. The magnitude of the tensile stress induced by the stress waves is of the order of ρcV and is sufficient to cause columnar fracture due to the lateral propagation of pre-existing flaws near the top of the coating. The role played by the geometry of the columns and the contact angle between the indenter and coating are explored. It remains to determine the effect of an inclined impact event upon the likelihood of erosion: the shape of turbine blades is such that erosive particles can impinge the coating at an inclination rather than at normal incidence. This is a topic of future study.

This research was supported by a program of international collaboration between the National Science Foundation (DMR-0099695) and the European Commission (*HIPERCOAT:* GRD2-200-30211). Funding from the US Office of Naval Research (contract N00014-05-1-0375) is also gratefully acknowledged.

References

[1] R.A. Miller: J. Am. Ceram Soc. 67 (1984) 517–524.
[2] J.A. Ruud, A. Bartz, M.P. Borom, C.A. Johnson: J. Am. Ceram Soc. 84 (2001) 1545–1552.
[3] A.G. Evans, D.R. Mumm, J.W. Hutchinson, G.H. Meier, F.S. Pettit: Prog. Mater. Sci. 46 (2001) 505–553.
[4] A.M. Karlsson, J.W. Hutchinson, A.G. Evans: J. Mech. Phys. Solids 50 (2002) 1565–1589.
[5] D.R. Mumm, A.G. Evans, I.T. Spitsberg: Acta Mater. 49 (2001) 2329–2340.
[6] S.R. Choi, J.W. Hutchinson, A.G. Evans: Mech. of Mater. 31 (1999) 431–447.
[7] P.K. Wright, A.G. Evans: Curr. Opinion in Sol. State Mater. Sci. 4 (1999) 255–268.
[8] X. Chen, R. Wang, N. Yao, A.G. Evans, J.W. Hutchinson, R.W. Bruce: Mater. Sci. Eng. A 352 (2003) 221–231.
[9] J.R. Nicholls, M.J. Deakin, D.S. Rickerby: Wear 233 (1999) 352–361.
[10] R.G. Wlmann, J.R. Nicholls: Wear 242 (2000) 89–96.
[11] X. Chen, M.Y. He, I. Spitsberg, N.A. Fleck, J.W. Hutchinson, A.G. Evans: Wear 256 (2004) 735–746.
[12] X. Chen, J.W. Hutchinson, A.G. Evans: Acta Mater. 52 (2004) 565–571.
[13] A.G. Evans, N.A. Fleck, S. Faulhaber, N. Vermaak, M. Maloney, R. Darolia: Wear 260 (2006) 886–894.
[14] R.G. Welmann, M.J. Deakin, J.R. Nicholls: Wear 258 (2005) 349–356.
[15] K.L. Johnson: Contact Mechanics. Cambridge University Press 1985.
[16] L.B. Freund: Dynamic Fracture mechanics. Cambridge University Press 1990.
[17] J. Cole, J. Huth: J. Appl. Mech. 25 (1958) 433–436.
[18] J.W. Craggs, A.M. Roberts: J. Appl. Mech. 34 (1967) 207–209.
[19] L.M. Brock, H.G. Georgiadis: J. Thermal Stresses 23 (2000) 629–656.

(Received March 26, 2007; accepted September 9, 2007)

Bibliography

DOI 10.3139/146.101582
Int. J. Mat. Res. (formerly Z. Metallkd.)
98 (2007) 12; page 1196–1202

ISSN 1862-5282

Correspondence address

Prof. Norman A. Fleck
Cambridge University Engineering Dept.
Trumpington Street, Cambridge, CB2 1PZ, UK
Tel.: +44 1223 748 240
Fax: +44 1223 332 662
E-mail: naf1@eng.cam.ac.uk